Angle-dependent Face-centered SIBC Model of Metamaterial in Conformal FDTD Method

Samuel Gaucher, Christophe Guiffaut, Nicolas Bui, Alain Reineix, Olivier Cessenat

Angle-dependent Face-centered SIBC Model of Metamaterial in Conformal FDTD Method

Samuel Gaucher, Christophe Guiffaut, *Member, IEEE,* Nicolas Bui, Alain Reineix, *Member, IEEE,* and Olivier Cessenat

***Abstract*—To control the diffraction of a target illuminated by a radar wave, one technique is to consider periodics metamaterials. When they are applied as very thin heterogeneous layers on the surface of the target, the simulation by a full wave method based on meshed model has to deal with a multiscale problem, resulting in a huge amount of unknowns. This paper proposes to apply the metamaterial as an equivalent boundary condition via the Leontovich formula. The frequency-angle-polarization-dependent model is integrated on the surface target with a conformal FDTD resolution method. To establish the surface impedance model, a pattern of the metamaterial is modelled with periodic boundary conditions. The Spectral FDTD scheme is retained because existing numerical models developed for the FDTD method can be easily adapted to this method. Then, the CFL condition of the Spectral FDTD method is not restrictive and is the one given by the standard Yee scheme. The accuracy of the new scheme is first compared with the full material FDTD meshing and the Cartesian SIBC model when the target is a plate or a cube. Finally, the computational efficiency of the proposed SIBC model is evaluated on a cylinder with comparisons between FEKO, CST software and our homemade solver.**

***Index Terms*—Conformal FDTD, Metamaterial, AD-SIBC.**

I. Introduction

In this paper, an angle-dependent surface impedance boundary condition (AD-SIBC) of a periodic metamaterial is introduced on the surface of a 3D target modeled in conformal FDTD. Accordingly, the coating consisting of a metamaterial is not meshed. Then, the spatial mesh can be coarser. Indeed, full material meshing is supposed to be small enough to capture the field variations inside the thin layer of metamaterials. Since the latter is replaced by a SIBC model, the chosen spatial mesh can be larger because it is not governed anymore by the thin layer thickness. As a result, the cell number of the computational volume is reduced by α^3 and the computational time by α^4 where $\alpha = \Delta_{coarse}/\Delta_{fine}$ is the factor of relaxed meshing.

Manuscript received DATE, YEAR; accepted DATE, YEAR. Date of publication DATE, YEAR; date of current version DATE, YEAR. This work was supported in part by the Direction générale de l'armement, l'Agence de l'innovation de Défense; and in part by the Centre d'études Scientifiques et Techniques d'Aquitaine, Commissariat à l'Energie Atomique et aux Energies Alternatives. (Corresponding author: Samuel Gaucher.)

Samuel Gaucher is with the Centre d'études Scientifiques et Techniques d'Aquitaine, Commissariat à l'Energie Atomique et aux Energies Alternatives 33116, Le Barp, France, and also with the XLIM, Centre National de la Recherche Scientifique, 87000 Limoges, France (e-mail: samuel.gaucher@cea.fr; samuel.gaucher@xlim.fr).

Christophe Guiffaut, Nicolas Bui and Alain Reineix are with the XLIM, Centre National de la Recherche Scientifique, 87000 Limoges, France (email: christophe.guiffaut@xlim.fr, nicolas.bui@xlim.fr, alain.reineix@xlim.fr).

Olivier Cessenat is with the Centre d'études Scientifiques et Techniques d'Aquitaine, Commissariat à l'Energie Atomique et aux Energies Alternatives, 33116 Le Barp, France (email: olivier.cessenat@cea.fr).

Because the purpose is to calculate the radar cross section (RCS) of a large dimension target over a wideband, the FDTD method is a good condidate to solve the Maxwell equations. In a first step, Floquet periodic boundary conditions (PBC) are applied around the elementary pattern of the periodic metamaterial. For all incident angles and for both polarization TE and TM, the metamaterial surface impedances are computed with the Spectral FDTD scheme [1] [2] combined with an extrapolation technique TD-VFz [3] called the hybrid SFDTD/TD-VFz scheme [4]. SFDTD method is a good choice for at least two reasons. First, numerous known numerical techniques with Yee's scheme as dispersive media, thin plates and subcell models can be applied straighforwardly because SFDTD solves the electric field E and the magnetic field H contrary to the field transformation method [5] [6]. Second, no additional constraint is needed on the CFL criterion. Then, the hybridation with the TD-VFz technique efficiently solves the resonance problem inherent to the Spectral FDTD method to obtain accurate responses at high incidence [4].

In a second step, the frequency-dependent AD-SIBC model is also decomposed by the vector fitting (VF) technique [7] to efficiently process the time domain convolution product. Then, the model is introduced as a Leontovich boundary condition [8] on the target surface with a conformal resolution method. Conformal techniques [9] [10] are efficient solutions to drastically reduce staircase modeling errors. Our approach is based on the face-centered technique [11] [12] that allows us to project the magnetic field vector in the middle of conformal region for the AD-SIBC model processing.

The contents of this paper is organized as follows. The periodic structure is solved in Section II with the SFDTD+TD-VFz approach or with analytical formulas for simple stratified media. In Section III, the conformal angle-dependant SIBC model in the FDTD method is derived and deeply detailed as this part appears to be complex due to the need of several coordinate systems. First, in section III-A, the tangent electric field is computed using the Leontovich relation in each conformal region by taking into account the illumination angle of the plane wave. Then, in section III-B, the magnetic field is updated using Faraday's equation under contour integral form. In Section IV, three numerical examples are implemented to demonstrate the conformal AD-SIBC model performance. Implementation and numerical results are made with the TEMSI-FD solver [13] developed at XLIM institute. Our conformal FDTD approach is compared with the standard Yee scheme [14] where the metamaterial structure is fully meshed and to the Cartesian AD-SIBC approach [11] [12] when possible as with plate and cube surfaces. The last example is a cylinder

where the conformal AD-SIBC model is compared with the CST [15] and FEKO solvers [16]. Finally, Section V concludes this paper.

II. Periodic Structures Modeling

Complex metamaterials can be simulated with the SFDTD/TD-VFz method by introducing periodic boundary conditions around an elementary pattern of the periodic structure. The surface impedance is deduced for numerous samples from the angle ranges $(\theta,\ \varphi) \in [0°, 90°[^2$ and for both polarization TE and TM of an incident plane wave

$$Z_\varphi = -\frac{E_\varphi}{H_\rho} \text{ (TE mode)},\ Z_\rho = \frac{E_\rho}{H_\varphi} \text{ (TM mode)}. \quad (1)$$

Here, Z is the surface impedance and (ρ, φ) designates the axes of the cylindrical basis. Angles θ and φ are spherical angles. The main propagation direction is z such as the surface impedance plane is xy-plane or $\rho\varphi$-plane according to the coordinate system. These ratios are evaluated in free space on the xy-plane at the Yee half-cell distance from the air-material interface, which is still a very small distance compared to the wavelength. Thus, this slight shift has no significant impact on the impedance and allows direct free space interpolation of the $E-H$ fields at the middle of the Yee cells. Besides, (1) is obtained from an average of the $E-H$ fields over the entire xy-plane section of the elementary pattern.

To facilitate processing in the time domain, surface impedances Z are fitted by series of order 1 and 2 filters with the VF technique [7]

$$Z_{\varphi,\rho}(\omega,\theta,\varphi) = r_0^{\varphi,\rho} + \sum_{l=1}^{N_r^{\varphi,\rho}} \frac{k_l^{\varphi,\rho}}{j\omega - \omega_l^{\varphi,\rho}} + \sum_{l=1}^{N_c^{\varphi,\rho}} \left[\frac{a_l^{\varphi,\rho} + jb_l^{\varphi,\rho}}{j\omega - (c_l^{\varphi,\rho} + jd_l^{\varphi,\rho})} + \frac{a_l^{\varphi,\rho} - jb_l^{\varphi,\rho}}{j\omega - (c_l^{\varphi,\rho} - jd_l^{\varphi,\rho})} \right], \quad (2)$$

where N_r^φ (resp. N_r^ρ) is the number of first-order filters and N_c^φ (resp. N_c^ρ) is the number of second-order filters in the series expansion of Z_φ (resp. Z_ρ) at the fixed incidence (θ, φ), r_0 is the resistance, k_l and $a_l^{\varphi,\rho} \pm jb_l^{\varphi,\rho}$ the residus, ω_l and $c_l^{\varphi,\rho} \pm jd_l^{\varphi,\rho}$ the poles.

For example, Fig. 1 shows an elementary pattern of a periodic absorber. The metamaterial is composed of a FR4 substrate (blue) covered by ITO films (yellow) [17] and a ground plane to cancel electromagnetic (EM) transmission. The SFDTD+TD-VFz method is employed to compute this periodic structure. The metamaterial is illuminated by a plane wave propagating in the $-z$ direction. PBC are applied around the elementary pattern in the x and y directions. The convolution perfectly matched layers [18] are used in the z-direction to process the outgoing waves. The FDTD spatial steps for the simulation are all equal to $\Delta = 0.25$ mm and the associated CFL stability criterion is set to $CFL = 0.99$. In agreement with [17], Fig. 2 shows this absorber can achieve high absorption rate for the frequency band 1-18 GHz.

Note that for a simple homogenous stratified media, analytical surface impedances can be obtained with the Demarest solutions [19]. For the example of a ground plane covered by a dielectric layer $\epsilon_r = 4$ with loss $\sigma = 0.6\ S/m$ and thickness $d = 3\ mm$ called ground+diel+loss, Fig. 3 shows the TM polarization surface impedance magnitude and the 6 poles VF model one (2 real poles and 2 pairs of complex conjugated poles). As shown for three angles, VF responses are successfully fitted for all incident angles. Physical frequency shift and a decrease in amplitude are observed as the incident angle increases.

III. AD-SIBC in Conformal FDTD Method

The aim is to predict the RCS of a target with parts of metamaterials. The latter is replaced by the AD-SIBC model computed in section II.

A. Electric components update

The metamaterial interface often cuts the FDTD cell into two regions as shown in Fig. 4. The direct local basis (u, v, n)

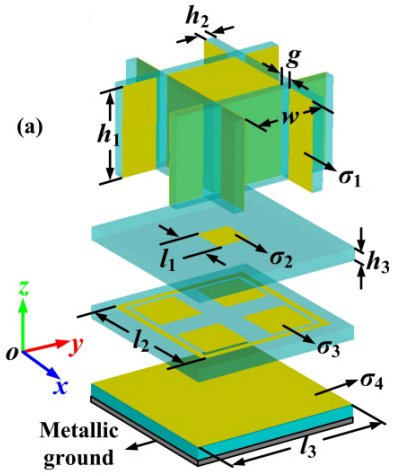

Fig. 1. Elementary pattern of the FR4+ITO absorber [17].

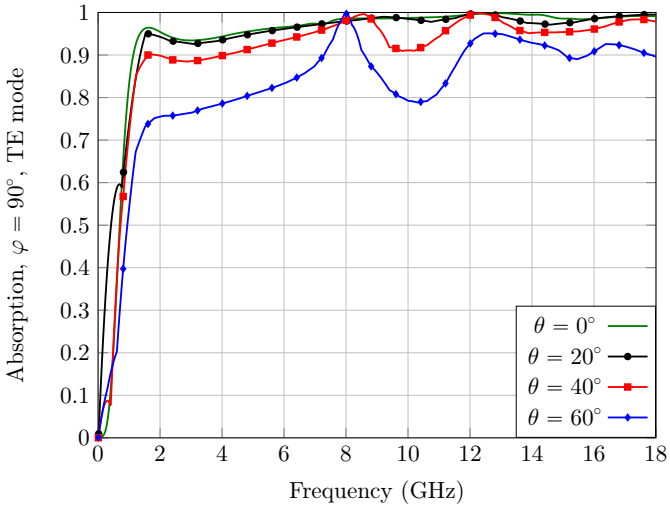

Fig. 2. Absorption rate of the FR4+ITO absorber obtained by the SFDTD+TD-VFz method.

is defined on the interface where n is the outgoing normal unit vector and (u, v) are two tangent unit vectors. Vector u can be chosen by the user to indicate the material orientation on the target especially when it has an anisotropic behaviour. Vector v is deduced by the cross product $v = n \times u$. The illumination angle must be known to apply the correct angle-dependent SIBC model. The latter is chosen for a single incident angle in each conformal region containing a metamaterial interface. Since only the plane wave incident angle is known, multiple interactions and shadow waves are not taken into account with this model. Now, the incident angle of the plane wave relative to the local basis (u, v, n) is derived. The local angle θ_n is the angle between the unit vector n and the unit vector $\vec{r} = \vec{k}/k_0$ along the incident axis where $k_0 = \omega/c$ is the wave number and $\vec{k}$ is the incident wave vector defined in Fig. 4. This yields

$$\vec{r}_{x,y,z} = \sin\theta\cos\varphi\ \vec{x} + \sin\theta\sin\varphi\ \vec{y} + \ \cos\theta\vec{z}, \qquad (3)$$

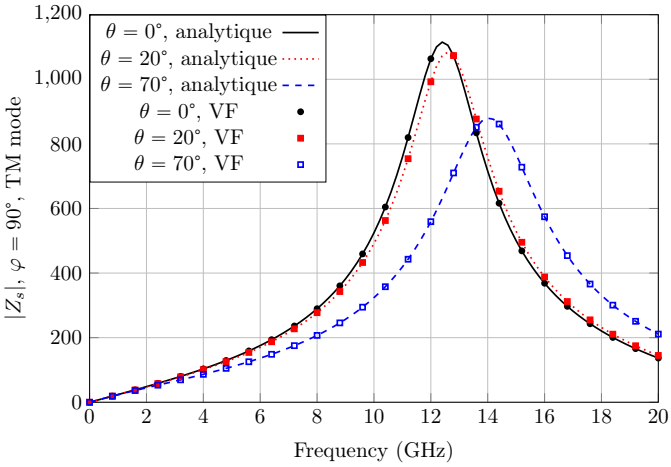

Fig. 3. Magnitude of analytical surface impedance of the ground+diel+loss for several incident angles.

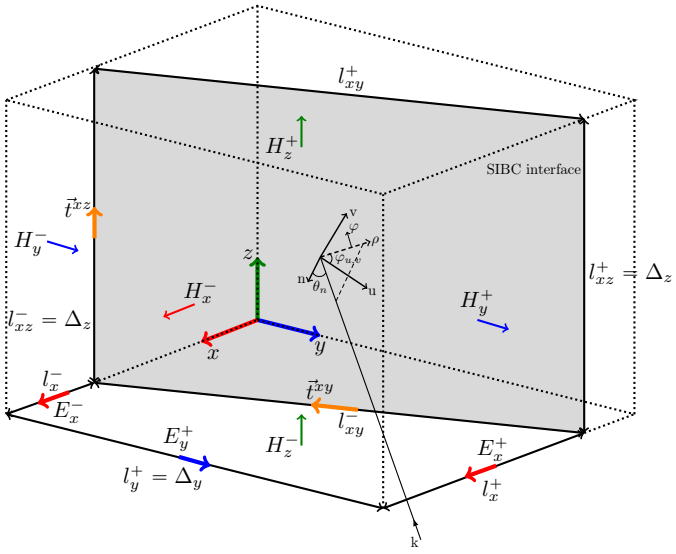

Fig. 4. Metamaterial interface cutting a Yee cell into two regions.

where θ and azimuth φ are the spherical angles in the global Cartesian basis (x, y, z). The local azimuth angle $\varphi_{u,v}$ is the angle between the unit vector u and the vector ρ which is the projection of the vector r in the local uv-plane. Then, the vector r in the local basis reads

$$r_u = \sin\theta_n \sin\varphi_{u,v},\ \ r_v = \sin\theta_n\cos\varphi_{u,v},\ \ r_n = \cos\theta_n. \quad (4)$$

The local angles are determined by the projection of the vector r in the local basis (u, v, n)

$$\vec{r}_{u,v,n} = r_u\ \vec{u} + r_v\ \vec{v} + r_n\ \vec{n},\quad r_u = r.u,\ \ r_v = r.v,\ \ r_n = r.n. \qquad (5)$$

Then, using (4), we obtain

$$\theta_n = \arccos r_n,\ \ \varphi_{u,v} = \arctan\frac{r_v}{r_u}. \qquad (6)$$

The tangential electric components in the cylindric coordinates (ρ, φ) are then deduced by the Leontovich relation

$$\begin{bmatrix} E_\rho \\ E_\varphi \end{bmatrix} = \begin{bmatrix} 0 & -Z_\rho(\omega, \theta_n, \varphi_{u,v}) \\ Z_\varphi(\omega, \theta_n, \varphi_{u,v}) & 0 \end{bmatrix} \begin{bmatrix} H_\rho \\ H_\varphi \end{bmatrix}. \quad (7)$$

Fig. 5 shows the correct model to be applied in the conformal region for the PEC circle. The local angle $\theta_n = 0°$ occurs in front of the circle when $k.n = -1$. Then, the absolute scalar product $|k.n|$ decreases until it becomes equal to $k.n = 0$ on the circle sidewalls. The shadow region $(k.n \geq 0)$ is represented by the dashed blue line.
Let $\mathcal{M}(\varphi_{u,v})$ be the transform matrix between the cylindrical coordinates (φ, ρ) and the local coordinates (u, v)

$$\mathcal{M}(\varphi_{u,v}) = \begin{bmatrix} \cos\varphi_{u,v} & \sin\varphi_{u,v} \\ -\sin\varphi_{u,v} & \cos\varphi_{u,v} \end{bmatrix}. \qquad (8)$$

Eq. (7) becomes

$$\begin{bmatrix} E_u \\ E_v \end{bmatrix} = \mathcal{M}^{-1}(\varphi_{u,v}) \begin{bmatrix} 0 & -Z_\rho \\ Z_\varphi & 0 \end{bmatrix} \mathcal{M}(\varphi_{u,v}) \begin{bmatrix} H_u \\ H_v \end{bmatrix}. \qquad (9)$$

Having only the Cartesian magnetic components (H_x, H_y, H_z) in the Yee cell, H-field projection in the local basis to

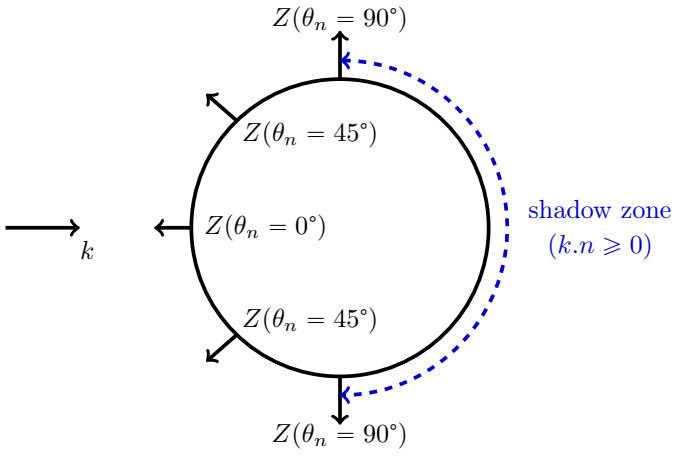

Fig. 5. Surface impedance choice in conformal regions for the circle case.

obtain (H_u, H_v) is required to update (E_u, E_v) in (9). For $u = (u_x, u_y, u_z)$, $v = (v_x, v_y, v_z)$, the projection reads

$$\begin{aligned} H_{u,v,n} &= H_u\ \vec{u} + H_v\ \vec{v} + H_n\ \vec{n}, && \text{(10a)} \\ H_u &= H_x u_x + H_y u_y + H_z u_z, && \text{(10b)} \\ H_v &= H_x v_x + H_y v_y + H_z v_z. && \text{(10c)} \end{aligned}$$

The tangential magnetic components (H_y, H_z) in (10) are approximated by their interpolated values. As shown in Fig. 4, they are given by the Yee scheme with H-components located on the adjacent Yee faces to the interface

$$\begin{aligned} H_y &\approx \frac{1}{2}\left(H_y^- + H_y^+\right), && \text{(11a)} \\ H_z &\approx \frac{1}{2}\left(H_z^- + H_z^+\right). && \text{(11b)} \end{aligned}$$

The component H_x is approximated by the single component located on the Yee face in front of the SIBC interface

$$H_x \approx H_x^-. \tag{12}$$

Then, the tangent electric components in the local basis are deduced by developping the right-hand side of (9)

$$\begin{aligned} E_u &= Z_\varphi H_1^{TE} + Z_\rho H_1^{TM}, && \text{(13a)} \\ E_v &= Z_\varphi H_2^{TE} + Z_\rho H_2^{TM}, && \text{(13b)} \end{aligned}$$

where

$$\begin{aligned} H_1^{TE} &= -\cos\varphi_{u,v}\sin\varphi_{u,v} H_u - \sin^2\varphi_{u,v} H_v, && \text{(14a)} \\ H_2^{TE} &= \cos^2\varphi_{u,v} H_u + \cos\varphi_{u,v}\sin\varphi_{u,v} H_v, && \text{(14b)} \\ H_1^{TM} &= \cos\varphi_{u,v}\sin\varphi_{u,v} H_u - \cos^2\varphi_{u,v} H_v, && \text{(14c)} \\ H_2^{TM} &= \sin^2\varphi_{u,v} H_u - \cos\varphi_{u,v}\sin\varphi_{u,v} H_v. && \text{(14d)} \end{aligned}$$

Now, we consider only the update of E_u (the E_v computation follows the same reasoning). With the impedance model (2), the following variables are introduced

$$\begin{aligned} V_{l,\varphi}^{o=1} &= \frac{k_l^\varphi}{j\omega - \omega_l^\varphi} H_1^{TE}, \\ V_{l,\rho}^{o=1} &= \frac{k_l^\rho}{j\omega - \omega_l^\rho} H_1^{TM}, \\ V_{l,\varphi}^{o=2} &= \left[\frac{a_l^\varphi + j b_l^\varphi}{j\omega - (c_l^\varphi + j d_l^\varphi)} + \frac{a_l^\varphi - j b_l^\varphi}{j\omega - (c_l^\varphi - j d_l^\varphi)}\right] H_1^{TE}, \\ V_{l,\rho}^{o=2} &= \left[\frac{a_l^\rho + j b_l^\rho}{j\omega - (c_l^\rho + j d_l^\rho)} + \frac{a_l^\rho - j b_l^\rho}{j\omega - (c_l^\rho - j d_l^\rho)}\right] H_1^{TM}, \end{aligned}$$

to obtain

$$E_u = R_0 + \sum_{l=1}^{N_r^\varphi} V_{l,\varphi}^{o=1} + \sum_{l=1}^{N_r^\rho} V_{l,\rho}^{o=1} + \sum_{l=1}^{N_c^\varphi} V_{l,\varphi}^{o=2} + \sum_{l=1}^{N_c^\rho} V_{l,\rho}^{o=2}, \tag{16}$$

where

$$R_0 = r_0^\varphi H_1^{TE} + r_0^\rho H_1^{TM}. \tag{17}$$

The tangent component E_u and the auxiliary variables V are computed at the same time $t^n = n\Delta_t$. However, this is not the case for the magnetic field variables H_1^{TE} and H_1^{TM} carried by r_0^φ and r_0^ρ respectively in (17). Indeed, Yee's leapfrog scheme suggests a half step time shift for the computation of the magnetic components, i.e. only the $H^{n-\frac{1}{2}}$ components are stored in the computer memory. One could propose averaging solution to this problem but they will not improve the responses. In fact, the time variations are very slow and, therefore, the half step time shift leads to a minor error [20]. Therefore, the following simple temporal approximation is adopted

$$H_1^n \approx H_1^{n-\frac{1}{2}}. \tag{18}$$

For the auxiliary variables V in (16), each order 1 filter requires one unknown of the discrete problem while each order 2 filter requires two unknowns. Passive circuit scheme is retained for solving auxiliary variables. Since order $o = 1$ filter is equivalent to a RC circuit and order $o = 2$ filter to a RLC circuit [21], a discretization at time $(n - \frac{1}{2})\Delta_t$ for the order 1 components $V \equiv V_{l,\varphi}^{o=1}$ and $V \equiv V_{l,\rho}^{o=1}$ leads to the following relationship with an exponential type scheme [22], [23]

$$V^n = \alpha V^{n-1} + R\,(1-\alpha)\, I^{n-\frac{1}{2}}, \tag{19}$$

with $\alpha = \exp\left[-\dfrac{\Delta_t}{RC}\right]$, $R = -k_l\omega_l^{-1}$, $C = k_l^{-1}$ and $I \equiv H_1^{TE}$ for the $V_{l,\varphi}$ update or $I \equiv H_1^{TM}$ for the $V_{l,\rho}$ update. For auxiliary variables $V \equiv V_{l,\rho}^{o=2}$ and $V \equiv V_{l,\varphi}^{o=2}$ of order 2

$$V^n = \gamma V^{n-1} + R\,(1-\gamma)\,(I - I_L)^{n-\frac{1}{2}}, \tag{20}$$

where the I_L current exponential discretization at time $n\Delta_t$ reads

$$I_L^{n+\frac{1}{2}} = \beta I_L^{n-\frac{1}{2}} + \frac{1}{R_L}(1-\beta)\, V^n, \tag{21}$$

and

$$\begin{aligned} \gamma &= \exp\left[-\frac{\Delta_t}{R_2 C_2}\right], && \text{(22a)} \\ \beta &= \exp\left[-\frac{R_L \Delta_t}{L}\right], && \text{(22b)} \\ C_2 &= \frac{1}{2a_l}, && \text{(22c)} \\ R_2 &= \frac{2a_l^2}{b_l d_l - a_l c_l}, && \text{(22d)} \\ L &= \frac{2a_l}{d_l^2\left[1 + \left(\dfrac{b_l}{a_l}\right)^2\right]}, && \text{(22e)} \\ R_L &= -L\left(c_l + \frac{b_l d_l}{a_l}\right). && \text{(22f)} \end{aligned}$$

Now the auxiliary variables are updated with (19) and (20), the tangent electric field E_u in (16) can be computed. Then, its projection on the metamaterial edges of the conformal FDTD grid is applied. We note $t^{x,y}$ (resp. $t^{x,z}$) the unit vector in the edge direction on the xy-face (resp. xz-face) as shown in fig. 4. These edge vectors are oriented counterclockwise for the electric field contour integral computation i.e the scalar products $t^{x,y}.(n \times z)$ and $t^{x,z}.(n \times y)$ must be positive. The tangential electric components computed in the middle of the conformal region and oriented in the edge direction

are obtained by the projection of $E_{u,v,n}$ on the edge vector $t = (t_u, t_v, t_n = 0)$ expressed in the local basis

$$E^{x,y} = E_{u,v,n}.t^{x,y}_{u,v,n} = E_u t^{x,y}_u + E_v t^{x,y}_v, \quad (23a)$$
$$E^{x,z} = E_{u,v,n}.t^{x,z}_{u,v,n} = E_u t^{x,z}_u + E_v t^{x,z}_v, \quad (23b)$$
$$t_u = t_x u_x + t_y u_y + t_z u_z, \quad (23c)$$
$$t_v = t_x v_x + t_y v_y + t_z v_z. \quad (23d)$$

These new edge components close the electrical loops in the Cartesian conformal plane and provide a direct solution for the magnetic field in the conformal region.

B. Magnetic components update

The electrical contribution of the SIBC interface comes as a correction of the conformal PEC scheme for the magnetic components computation. For example, the H_z^- update in Fig. 4 without the SIBC interface contribution reads

$$\left(H_z^{n+\frac{1}{2}}\right)^- = \left(H_z^{n-\frac{1}{2}}\right)^- - \frac{\Delta_t}{\mu A_z^-}\Big[(E_x^n)^- l_x^- + (E_y^n)^+ l_y^+ - (E_x^n)^+ l_x^+\Big], \quad (24)$$

where A_z^- denotes the free area of the conformal face region with normal z containing H_z^-, and l_x, l_y are the conformal edge region lengths along x and y-directions respectively. Then, the tangential electric field computed in the middle of the SIBC interface and along the edge vector $t^{x,y}$ (23a) has 0.5 weight contribution on H_z^-. The correction becomes

$$\left(H_z^{n+\frac{1}{2}}\right)^- = \left(H_z^{n+\frac{1}{2}}\right)^- + \frac{\Delta_t}{2\mu A_z^-} E^{x,y} l^-_{x,y}, \quad (25)$$

where l^-_{xy} is the length of the metamaterial edge on the inferior xy-plane. The other half-contribution is provided by the tangent electric field coming from the cell below.
Following the same reasoning for H_z^+, this yields

$$\left(H_z^{n+\frac{1}{2}}\right)^+ = \left(H_z^{n+\frac{1}{2}}\right)^+ + \frac{\Delta_t}{2\mu A_z^+} E^{x,y} l^+_{x,y}. \quad (26)$$

In the same way, the tangential electric field computed in the middle of the SIBC interface and along the edge vector $t^{x,z}$ (23b) has 0.5 weight contribution on the two magnetic components H_y^- and H_y^+ near the interface

$$\left(H_y^{n+\frac{1}{2}}\right)^- = \left(H_y^{n+\frac{1}{2}}\right)^- - \frac{\Delta_t}{2\mu A_y^-} E^{x,z} l^-_{x,z}, \quad (27)$$
$$\left(H_y^{n+\frac{1}{2}}\right)^+ = \left(H_y^{n+\frac{1}{2}}\right)^+ - \frac{\Delta_t}{2\mu A_y^+} E^{x,z} l^+_{x,z}. \quad (28)$$

Finally, H_x^- is classically updated with the Yee scheme by the surrounding electric components E_z and E_y. For small conformal area, potential instabilities are corrected by increasing area according to the Benkler technique [9].

IV. Numerical results

This section presents three targets: an inclined plate, a cube and a cylinder. For the two first cases, the conformal AD-SIBC model results are compared with the FDTD reference using the Yee algorithm with a fully meshed structure and the Cartesian AD-SIBC reference model. For the cylinder case, conformal AD-SIBC model is compared with CST using its time finite integration technique and also with FEKO using its MOM method. We also plot the PEC model to exhibit the coating effect. The surface impedances are fitted by VF with 6 poles which is sufficient to obtain a good approximation.

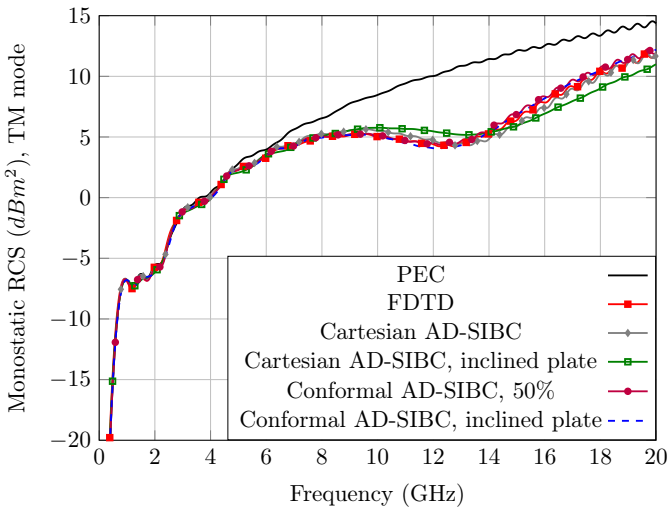

Fig. 6. Monostatic RCS obtained by the conformal AD-SIBC model in TM polarization for the inclined plate.

A. Inclined plate

Consider an inclined PEC plate of size $15\ cm \times 15\ cm$ covered by the ground+diel+loss described in section II. The unit tangent vector chosen is $u = +y$. Then, the incident vector k is normal to the inclined plate and is set to ($\theta = 70°$, $\varphi = 0°$). An uniform spatial step $\Delta = 1\ mm$ is applied and the CFL condition is set to $CFL = 0.5$. Fig. 6 shows an excellent agreement between the face-centered conformal AD-SIBC model and the references for the TM polarization monostatic RCS. Note that for the FDTD and Cartesian AD-SIBC references, the plate is not inclined and is located on the Yee cell yz-plane. Moreover, the conformal AD-SIBC 50% in the legend texbox corresponds to the case where the plate is also in the yz-plane but translated along x-direction of 50% of cell size such that the plate is located exactly in the Yee cells middle. As expected at low frequencies, the metamaterial behaves as a PEC one. Above 8 GHz, attenuation of RCS is observed with a maximum around 13 GHz corresponding to the resonant frequency in Fig. 3. The Cartesian AD-SIBC for an inclined plate (green curve) is obtained by a staircase mesh of the plate. In this case, two incidences are applied; $\theta_n = 70°$ for the xy stair and $\theta_n = 20°$ for the yz stair. As a result, the RCS is degraded at high frequencies that shows the interest of using the conformal technique.

B. Cube turned in azimuth

1) Cube covered by the ground+diel+loss: For the references calculation, the problem consists in a PEC cube covered by the ground+diel+loss on its two inferior xy and xz-faces. The PEC cube side length is $L = 8\ cm$. The cube is

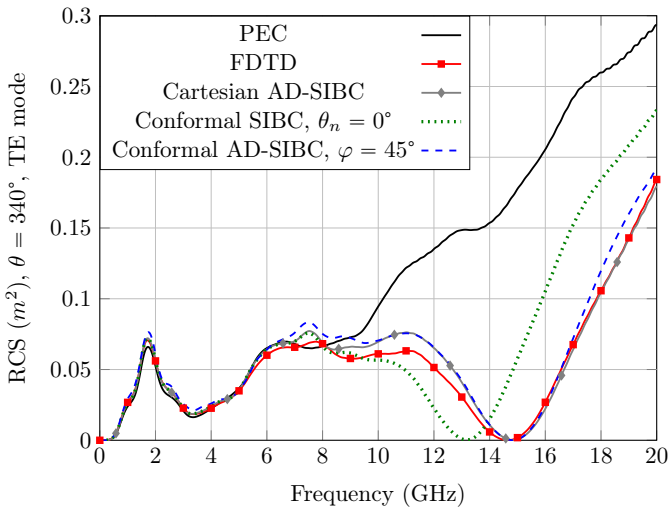

Fig. 7. RCS in the direction of reflectivity of the cube left face (which is in the direct radar visibility) for the ground+diel+loss cloaking.

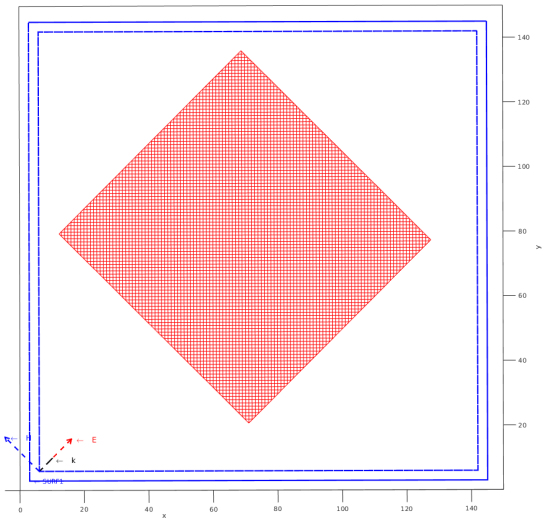

Fig. 8. Top view of the cube turned in azimuth (TEMSI-FD viewer).

illuminated by an incident plane wave of incidence ($\theta = 20°$, $\varphi = 90°$). The two faces covered by the material are in direct visibility of the incident ray. Spatial discretization steps are all set to $\Delta = 0.5\ mm$ for the references and two times coarser $\Delta = 1\ mm$ for the conformal AD-SIBC case. Then, the CFL condition is set to $CFL = 0.99$ for the reference and $CFL = 0.5$ for the conformal scheme. For the references, Fig. 7 illustrates the RCS for the TE polarization in the direction of reflectivity of the inferior xz-face (which is in the direct radar visibility). The legend $\varphi = 45°$ corresponds to the conformal case where the cube is turned in azimuth by $45°$ with its corresponding rotated incident plane wave (see Fig. 8). It is noted that the conformal AD-SIBC response follows the reference one but with a low increase on the amplitude at frequencies $f > 6$ GHz compared to the references. In addition, the RCS has also been computed by a conformal SIBC model that incorrectly takes into account the incident wave orientation (green dashed curve) with a local angle fixed at $\theta_n = 0°$ in each conformal region. As a result, a large frequency shift is observed with this simplified model using a normal SIBC approximation when comparing with the reference models. This demonstrates the necessity in this case to consider an angle-dependent SIBC model. This last result is expected from Fig. 3 which shows an impedance shifting to low frequencies when incident angle decreases. Regarding the CPU time, FDTD and AD-SIBC Cartesian references are around 34 minutes whereas the conformal FDTD technique is only around 5 minutes due to the spatial step reduction by two. Also, the memory usage is 0.686 GB for the conformal FDTD method, 1.29 GB for the AD-SIBC Cartesian reference and 1.85 GB for the FDTD case. The computations are performed with a 16 × Intel Core i9-9880H CPU @ 2.30 GHz processor with 1 CPU core.

2) Ground+diel+loss located in the shadow zone: The PEC cube is covered by the ground+diel+loss on its two inferior xy and xz-faces. The incidence comes from the top right side of the computational domain ($\theta = 160°$, $\varphi = 270°$) such that the inferior covered xy and xz-faces are located in the shadow zone. The angle-dependant model is not applicable in the conformal regions of the coating because they are not in the direct radar visibility. To know which appropriate model to choose, the PEC condition or the SIBC model with a local angle $\theta_n = 0°$, $\theta_n = 40°$ or $\theta_n = 80°$ is applied on both inferior shadow xy and xz-faces. Here, the case $\theta_n = 80°$ is considered as the grazing incidence impedance model. The reference is the fully FDTD meshed coating. The RCS is computed in the directions $\Omega = (\theta \in [0°, 360°], \varphi = 0°$ and $\varphi = 90°)$ so in both the yz and xz-planes. For several samples of the frequency band $0^+ - 10$ GHz, the relative error

$$Error = \frac{||\text{RCS}_{\text{FDTD reference}} - \text{RCS}_{\text{PEC or SIBC model}}||_{L^2(\Omega)}}{||\text{RCS}_{\text{FDTD reference}}||_{L^2(\Omega)}}. \tag{29}$$

is computed for the TM polarization. Fig. 9 shows that the error is very high when the coating is replaced by the PEC condition. The error even attains 30% for frequencies around 8 GHz. It is clear that it is more interesting to replace the coating with its SIBC model. Also, the θ_n grazing angle choice in the conformal regions minimizes the error which is around 5% for the whole frequency band. This behaviour can probably be explained by the fact that the waves propagating in the shadow zone are creeping waves around the cube.

3) Cube covered by the FR4+ITO absorber: The PEC cube size is 39 $cm \times 39\ cm$. It is covered on both inferior xy and xz-faces of the wideband absorber $1 - 18\ GHz$ of Fig. 1. This corresponds to 10 periods of the elementary pattern on both sides. The spatial step is uniform $\Delta = 2.5\ mm$ and the maximum frequency chosen is $f_{max} = 10\ GHz$. The structure is illuminated by an incident angle $\theta = 30°$. The cube and the azimuth angle are also turned with $\varphi = 45°$ for the conformal AD-SIBC scheme (as in Fig. 8). Fig. 10 shows that the RCS obtained by the conformal AD-SIBC model for the TE polarization and in the direction of reflectivity of the inferior xz-face is in excellent agreement with the Cartesian

AD-SIBC reference model. According to the Fig. 2, the RCS should decreases at frequencies $f > 1\ GHz$. Moreover, for $f \approx 8\ GHz$, the RCS is greatly reduced, which perfectly corresponds to the absorption peak observed in Fig. 2. Note that the FDTD reference is not given here due to the difficulty of meshing many small patterns on the cube. This multiscale problem implies a huge amount of computational resources.

C. Cylinder

As shown in Fig. 11, the last example is a PEC cylinder (orange) of height $L = 0.8\ m$ with radius $R = 0.4\ m$ covered by a dielectric layer (blue) $\epsilon_r = 12$ of thickness $3\ cm$ and a very thin resistive film $\sigma = 3e4\ S/m$ of thickness $d = 50\ nm$ (purple). The reflection coefficient R of this cloaking (infinite ground plane covered by the dielectric and the film) is given on Fig. 12. A behavior near the PEC model

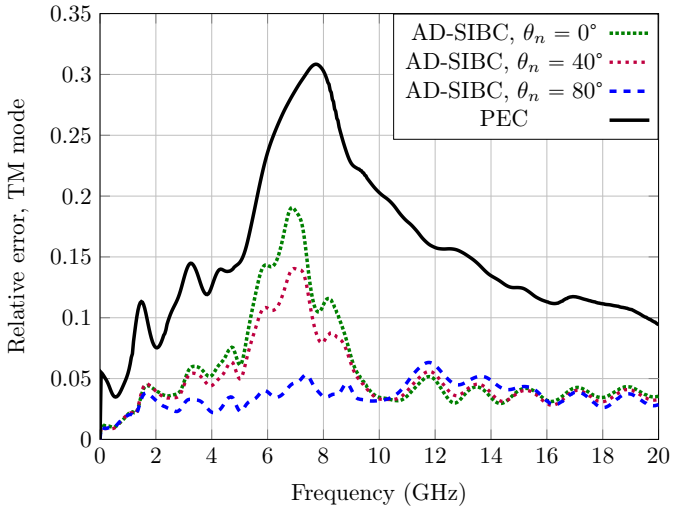

Fig. 9. Relative error obtained when replacing the coating with a PEC condition or a SIBC model.

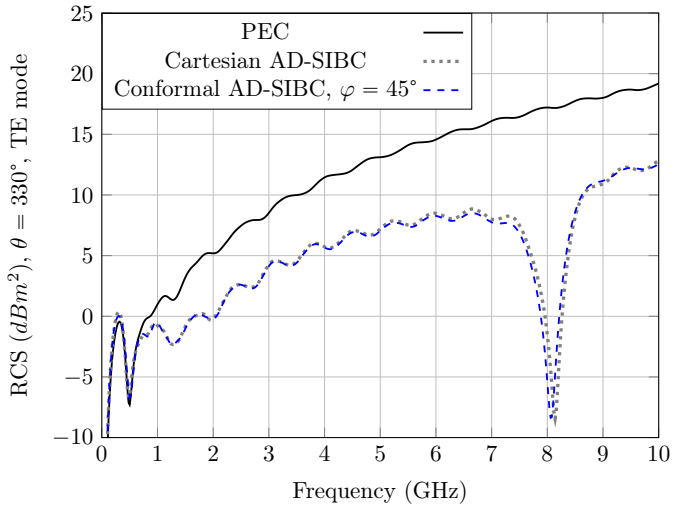

Fig. 10. RCS in the direction of reflectivity of the cube left face (which is in the direct radar visibility) for the ITO+FR4 metamaterial cloaking.

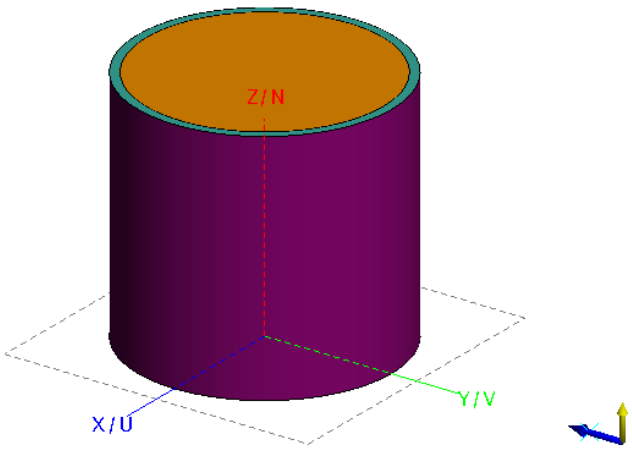

Fig. 11. FEKO vizualisation of the PEC cylinder covered by a material. The incident vector k is in blue color. The electric field is along the z-direction (yellow color vector) for the TM mode.

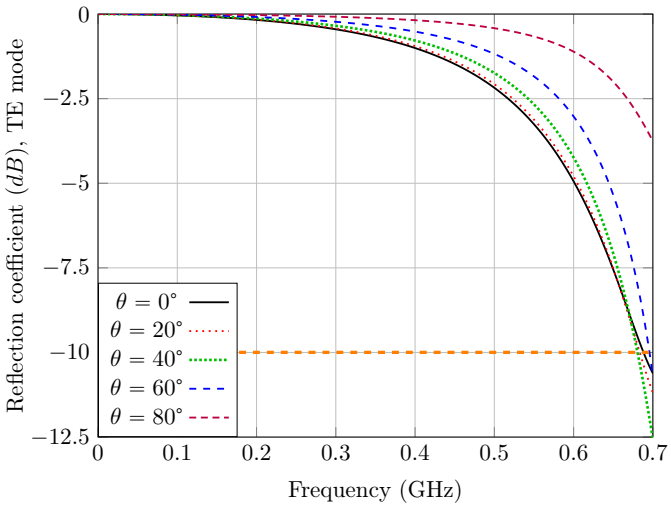

Fig. 12. Reflection coefficient of the cylinder cloaking for the TE mode.

is expected at low frequencies and a high RCS reduction near the maximal frequency $f = 700$ MHz of interest. At the maximal frequency, the cloaking is below the orange dotted line $R = -10\ dB$ which corresponds to an absorption rate better than 90%. The cylinder is illuminated by an incident plane wave of incidence ($\theta = 90°$, $\varphi = 90°$). The unit tangent vector chosen is $u = +z$, the spatial step $\Delta = 3\ cm$ and the $CFL = 0.7$. The monostatic RCS obtained by the conformal AD-SIBC model is compared with the FEKO and CST reference solvers for the TE and TM polarization as shown in Fig. 13 and Fig. 14 respectively. The FEKO solver uses the method of moment (MoM) with a standard meshing for 28 frequencies between 25 MHz to 700 MHz. For the CST solver, the conformal FDTD technique is used with a nonuniform mesh approximatively $\Delta_{CST} \approx 1\ cm$ and with a CFL condition set to $CFL = 0.95$. The dielectric layer and the resistive film are meshed. The latter is modeled by applying an equivalent conductivity $\sigma^{new} = \sigma d^{new}/\Delta_{CST}$

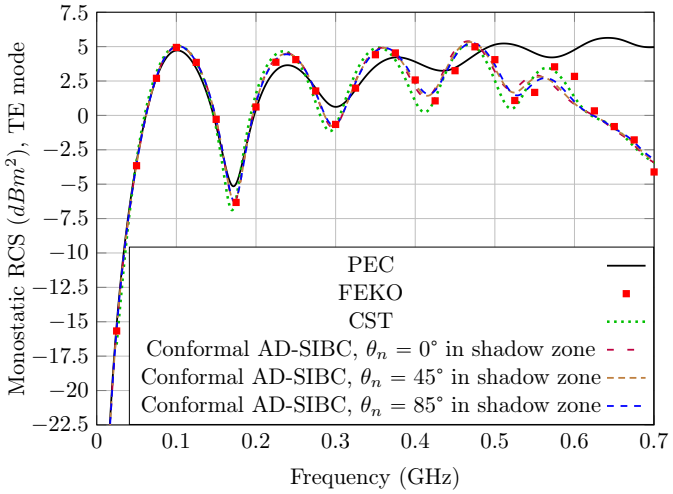

Fig. 13. Monostatic RCS of the cylinder for the TE polarization.

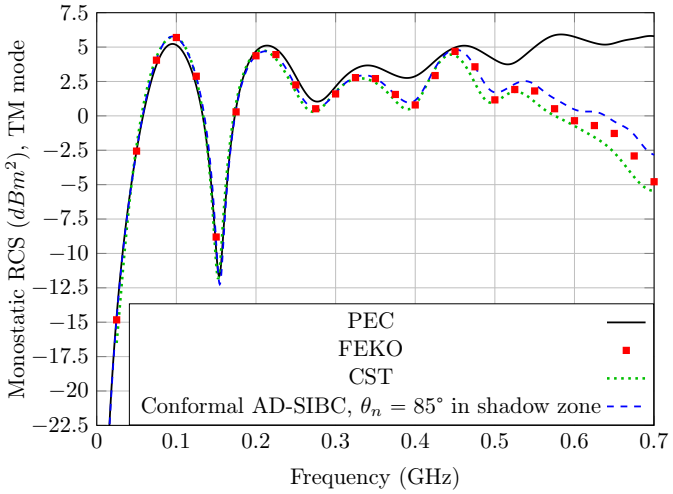

Fig. 14. Monostatic RCS of the cylinder for the TM polarization.

for the thickness $d^{new} = 0.5\ mm$. For the TE and TM polarizations, the conformal AD-SIBC model is in very good agreement with the references. A grazing incidence $\theta_n = 85°$ is applied in each shadow conformal region. This choice gives a better matching with the references, especially for the high frequencies RCS lobes as shown in Fig. 15 which shows a zoom on the top of the frequency band. Regarding the CPU time, wideband temporal methods are around 1 minute with 20 cores on 2 CPUs for the CST solver and 1 core for the proposed conformal FDTD method. For the 28 frequencies computation for FEKO, the CPU time is 12.3 hours for 8 cores on 1 CPU. Also, the memory usage is 0.112 GB for the conformal FDTD method, 1.7 GB for the CST reference and 21.802 GB (2.725 GB per core) for the FEKO case.

V. Conclusion

The angle-dependent face-centered SIBC model is a good candidate to solve multiscale problems with an absorbing metamaterial on the target. First, the technique is really computationally adapted for wideband response. Second, the FDTD poor geometry approximation by a staircase mesh is corrected by using the conformal FDTD method. Third, the method takes into account the primary oblique incident angle and both its polarization TE or TM. However, this technique is not applicable in shadow zone or when multiples interactions occurs like in cavity problems. Nevertheless, a grazing-angle SIBC model appears to be the best choice for the shadow zone. The use of a high-order impedance condition [24] could take these phenomena into account and this will be an interesting challenge for numerical methods in the time domain.

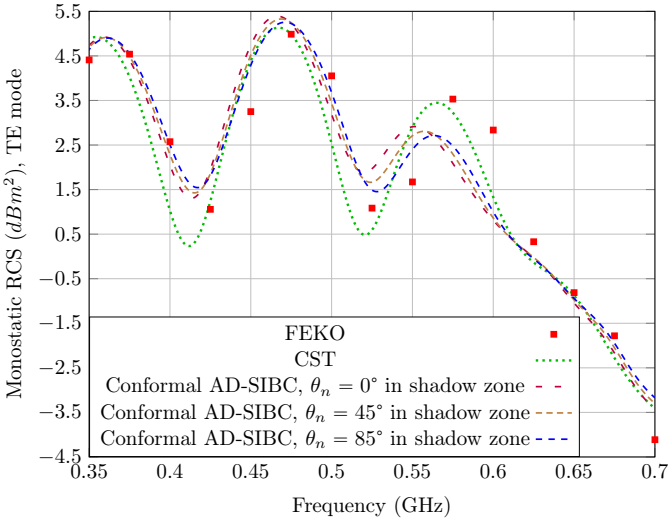

Fig. 15. Zoom on the top of the frequency band of Fig. 13.

References

[1] A. Aminian and Y. Rahmat-Samii, "Spectral FDTD: A novel technique for the analysis of oblique incident plane wave on periodic structures," *IEEE Trans. Antennas Propag.*, vol. 54, no. 6, pp. 1818–1825, 2006.

[2] F. Yang, J. Chen, R. Qiang, and A. Elsherbeni, "A simple and efficient FDTD/PBC algorithm for scattering analysis of periodic structures," *Radio Science*, vol. 42, no. 04, pp. 1–9, 2007.

[3] C.-U. Lei and N. Wong, "Efficient linear macromodeling via discrete-time time-domain vector fitting," in *21st International Conference on VLSI Design (VLSID 2008)*. IEEE, 2008, pp. 469–474.

[4] S. P. Gaucher, C. Guiffaut, A. Reineix, O. Cessenat, and G. Maze-Merceur, "Wideband simulations of periodic structures by the Hybrid Spectral FDTD/TD-VFz Method," *IEEE Antennas Wireless Propag. Lett.*, 2022.

[5] B. Liang, M. Bai, H. Ma, N. Ou, and J. Miao, "Wideband analysis of periodic structures at oblique incidence by material independent FDTD algorithm," *IEEE Trans. Antennas Propag.*, vol. 62, no. 1, pp. 354–360, 2013.

[6] J. Wang, J. Wang, B. Zhou, Q. Wu, B. Chen, L. Shi, and C. Gao, "Efficiency-improved 3-D WCS-FDTD algorithm for periodic structures at oblique incidence," *IEEE Antennas Wireless Propag. Lett.*, vol. 14, pp. 962–965, 2015.

[7] B. Gustavsen and A. Semlyen, "Rational approximation of frequency domain responses by vector fitting," *IEEE Transactions on power delivery*, vol. 14, no. 3, pp. 1052–1061, 1999.

[8] A. Guglielmi, "On the leontovich boundary condition in geoelectromagnetism," *Izvestiya, Physics of the Solid Earth*, vol. 45, no. 9, pp. 740–743, 2009.

[9] S. Benkler, N. Chavannes, and N. Kuster, "A new 3-D conformal PEC FDTD scheme with user-defined geometric precision and derived stability criterion," *IEEE Trans. Antennas Propag.*, vol. 54, no. 6, pp. 1843–1849, 2006.

[10] T. Xiao and Q. H. Liu, "Enlarged cells for the conformal FDTD method to avoid the time step reduction," *IEEE Microw. Wireless Compon. Lett.*, vol. 14, no. 12, pp. 551–553, 2004.

[11] C. Guiffaut, E. Perrin, F. Tristant, F. Terrade, and A. Reineix, "Modèles de parois conductrices dans la méthode fdtd appliquées à la problématique cem aéronautique," in *17ème Colloque International et Exposition sur la Compatibilité Electromagnétique*, Clermont-Ferrand, France, 30/06-03/07, 2014.

[12] I. D. Flintoft, S. A. Bourke, J. F. Dawson, J. Alvarez, M. R. Cabello, M. P. Robinson, and S. G. Garcia, "Face-centered anisotropic surface impedance boundary conditions in FDTD," *IEEE Transactions on Microwave Theory and Techniques*, vol. 66, no. 2, pp. 643–650, 2017.

[13] *Time ElectroMagnetic Simulator-Finite Difference Software, TEMSI-FD, CNRS, Univ. Limoges, Limoges, France*, 2006.

[14] A. Taflove and S. C. Hagness, *Computational electrodynamics: the finite-difference time-domain method*, 3rd ed. Artech house, 2005.

[15] C. M. STudio, "CST Studio Suite 2011," *Comput. Simul. Technol. AG*, 2014.

[16] M. Schoeman, J. Van Tonder, M. Bingle, U. Jakobus, E. A. Attardo, F. Cátedra, E. Garcia, and C. Delgado, "New Features in Altair Feko 2021," in *2021 International Applied Computational Electromagnetics Society Symposium (ACES)*. IEEE, 2021, pp. 1–2.

[17] C.-Y. Wang, J.-G. Liang, T. Cai, H.-P. Li, W.-Y. Ji, Q. Zhang, and C.-W. Zhang, "High-performance and ultra-broadband metamaterial absorber based on mixed absorption mechanisms," *IEEE Access*, vol. 7, pp. 57 259–57 266, 2019.

[18] J. A. Roden and S. D. Gedney, "Convolution PML (CPML): An efficient FDTD implementation of the CFS–PML for arbitrary media," *Microwave and optical technology letters*, vol. 27, no. 5, pp. 334–339, 2000.

[19] K. Demarest, R. Plumb, and Z. Huang, "FDTD modeling of scatterers in stratified media," *IEEE Trans. Antennas Propag.*, vol. 43, no. 10, pp. 1164–1168, 1995.

[20] M. Jansson, S. Ljung, M. Backstrom, and B. Wahlgren, "Efficient implementation of a submodel for composite materials to be combined with the FDTD-algorithm," *IEEE transactions on magnetics*, vol. 30, no. 5, pp. 3188–3191, 1994.

[21] E. Steenput, "A spice circuit can be synthesised with a specified set of s-parameters," *Vrije Universiteit Brussel*, pp. 1–12, 1999.

[22] P. G. Petropoulos, "Analysis of exponential time-differencing for FDTD in lossy dielectrics," *IEEE Trans. Antennas Propag.*, vol. 45, no. 6, pp. 1054–1057, 1997.

[23] J.-P. Bérenger, "Comparison of the Standard Differencing With the Exponential Differencing for the FDTD Method in Lossy Media," *IEEE Journal on Multiscale and Multiphysics Computational Techniques*, vol. 3, pp. 295–302, 2018.

[24] B. Stupfel, P. Payen, and O. Lafitte, "A Well-Posed and Effective High-Order Impedance Boundary Condition for the Time-Harmonic Scattering Problem from a Multilayer Coated 3-D Object," *Progress In Electromagnetics Research B*, vol. 94, pp. 127–144, 2021.

Samuel Gaucher was born in Tours, France, in 1994. He received the master's degree in advanced mathematics from the University of Tours, Tours, in 2018 and in mathematics and applications from the University of Nantes, Nantes, in 2019. He is currently pursuing the Ph.D. degree with the CEA CESTA laboratory, Le Barp, France, and the XLIM Laboratory, University of Limoges, Limoges, France. His Ph.D. thesis research field includes the development and the implementation of a metamaterial model in a conformal FDTD code.

Christophe Guiffaut was born on March 14, 1973 in Chateaubriant, France. He received the master's and Ph.D. degrees in electronics and telecommunications, in 1997 and 2000 respectively, from the University of Rennes, France. He joined the CNRS research center in 2002 and he integrated in the same year the XLIM laboratory at the University of Limoges, France. His research interests include the numerical methods in the time domain with various application areas such as EMC and Radar. Numerical Modeling developments concern cables, lightning and HIRF effects on aircraft and building, antennas and ground penetrating Radar.

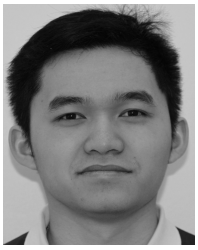

Nicolas Bui was born in Nantes, France, in 1989. He received the master's degree in mathematics and applications in 2012 from the University of Nantes, France. In 2016, he received the Ph.D degree in electronics, from the University of Limoges, France. Since 2017, He joined XLIM Laboratory as a Post-doctoral scientist at the University of Limoges, France. His research interests field includes the development of numerical methods in the time domain for applications in electromagnetic compatibility and scattering.

Alain Reineix was born in Neuvic-Entier, France, in 1961. He received the master's degree in electronics and telecommunications and the Ph.D. degree in electronics from the University of Limoges, Limoges, France, in 1984 and 1986, respectively. In 1986, he joined the Centre National de la Recherche Scientifique (CNRS) as a researcher with the IRCOM Laboratory, University of Limoges. Since 1991, he has been a Research Director with CNRS and also the Head of a Research Group on EMC, IRCOM Laboratory, and has been with XLIM Laboratory, University of Limoges, since 2006. His current research interests include improvements on numerical modeling particularly in FDTD for solving EMC problems and for ground penetration studies in the radar domain. He also works on the electromagnetic wave propagation in particular media such as over the sea for radars in the HF frequency range.
Pr. Reineix is a member of the French Electrical Engineering Society (SEE).

Olivier Cessenat was born in France in 1969. He qualified as an engineer from ENSAE aka Sup'Aero, Toulouse, in 1992. He received the Ph.D. degree in numerical analysis from the University of Paris IX Dauphine, France, in 1996. In 2003, he joined the CEA, Commissariat à l'Energie Atomique (French Atomic Energy Commission) near Bordeaux, France. His current research interests are electrodynamics and computer codes for physics on super computers.